

Charge screening effects in the resonant photoemission of Rh₂O₃, RuO₂, and MoO₂V. Stoeberl¹, E. B. Guedes², M. Abbate¹, F. Abud³, R. F. Jardim³ and R. J. O. Mossaneck^{1,*}¹*Departamento de Física, Universidade Federal do Paraná, Caixa Postal 19091, 81531-990 Curitiba, Brazil*²*Swiss Light Source, Paul Scherrer Institut, CH- 5232 Villigen, Switzerland*³*Instituto de Física, Universidade de São Paulo, Rua do Matão 1371, CEP 05508-090 São Paulo, Brazil*

(Received 24 July 2020; accepted 22 September 2020; published 12 October 2020)

We have performed valence-band resonant photoemission spectroscopy across the transition-metal (TM) L_3 edge of Rh₂O₃, RuO₂, and MoO₂. This technique allows us to access important information on the partial contribution of each respective TM. We show that an extended cluster model, coupled with transitions between discrete and continua states, describes well the overall resonance behavior as well as the experimental constant initial-state (CIS) spectra. Moreover, we analyze the resonant enhancement of the main lines and satellite structures to discuss the influence of the different charge regimes, the TM–O $2p$ hybridization, and additional charge screenings to the CIS signal. Finally, we argue that this approach can be extended to the study of other transition-metal oxides.

DOI: [10.1103/PhysRevB.102.155112](https://doi.org/10.1103/PhysRevB.102.155112)**I. INTRODUCTION**

Resonant photoemission spectroscopy (RPES) is a powerful technique to study the electronic structure of transition-metal oxides (TMO's) [1–4]. In principle, it allows one to identify and decompose the O $2p$ and transition-metal (TM) d partial contributions to the valence band (VB) of a given system, which are usually heavily mixed. The use of high photon energies also gives this method bulk sensitivity, which can be applied to interpret with an excellent agreement several physical properties of these TMO materials [5–8].

After identifying a coincidence in energies of different configurations that caused an atypical profile in the He atomic spectrum, Fano developed a theory to treat interactions between discrete and continuum states. Fano concluded that the interference between the two transition possibilities (to continuum and discrete autoionized states) generated the resonance profile presented by the helium spectrum (Fano line shape) [9]. Arguing about decay probabilities and matrix elements, Dietz *et al.* [10] was the first to explain Fano resonance occurring at the $3p$ threshold absorption. The interference was said to be occurring between the direct ($3p^6 3d^9 + h\nu \rightarrow 3p^6 3d^8 \epsilon f$) and indirect ($3p^6 3d^9 + h\nu \rightarrow 3p^5 3d^{10} \rightarrow 3p^6 3d^8 \epsilon f$) processes involving super-Coster-Kronig (SCK) [11,12] transitions, which gave rise to the characteristic Fano line shape.

After successfully expanding Fano's theory to study many discrete continua interactions [13], Davis and Feldkamp applied their formalism to RPES involving SCK transitions in solids [14]. They considered different models that illustrated various aspects of resonance behavior. Among other features, they investigated the difference in the $h\nu$ dependence of the mainline and satellite spectra, as well as the effect of interference on the line shapes, for a few $3d$ systems (Cr, Ni, Cu,

and Zn) [14]. Using a simple model including d - d Coulomb interaction and metal-ligand transitions [15], Davis performed a study about RPES in $3d$ transition-metal oxides and halides. His results presented a behavior qualitatively similar to the results reported by Oh *et al.* [16] for several nickel compounds. Main lines exhibited interference dips and the resonant enhancement occurred mostly in the satellite structures. The same trend was found for Ni compounds by Fujimori and Minami using a more complex cluster model [17].

Here, we aim to study the photon energy dependence of the intensities in the valence-band structure of $4d$ TMO's, as well as to reproduce the effect of the interference between direct and indirect photoemission processes illustrated by Fano line-shape curves. Since cluster model calculations have produced reliable results in the description of several TMO compound spectra [8,18–21], we propose to combine Davis and Feldkamp's extension of Fano's theory [14] with an extended cluster model to describe $4d$ TMO resonance within the L_3 ($2p_{3/2}$) absorption edge. To do so, we choose three TM $4d$ compounds with the following crystal structures and ionic fillings: Rh₂O₃ (a regular d^6 semiconductor), RuO₂ (a regular d^4 metal), and MoO₂ (a distorted d^2 metal). Our goal is to understand the role of charge-transfer (CT) and screening effects in the RPES description of these relatively simple oxides and to make this understanding possible for future applications in more complex systems.

II. EXPERIMENTAL DETAILS

Polycrystalline pellets of RuO₂ and MoO₂ oxides were obtained from commercial powders (99.9%) from Alfa Aesar. The synthesis of Rh₂O₃ consisted of consolidating finely divided rhodium powders, 99.9% pure from Alfa Aesar, into pellets and sintering them in a tubular oven heated in a slow stream of dry oxygen at 850 °C for 24 h.

The phase purity and crystal structure of the samples were confirmed by x-ray-diffraction (XRD) measurements,

*mossaneck@fisica.ufpr.br

performed in a Bruker D8 Discovery diffractometer. Rh_2O_3 crystallized in the orthorhombic (space group $Pbca$) structure, RuO_2 was formed in the rutile (space group $P4_2/mnm$) structure, and MoO_2 exhibited the distorted monoclinic (space group $P1\ 2_1/c\ 1$) symmetry. The XRD data refinements were also compared to previous reports [22–24], showing an excellent agreement.

The spectroscopic measurements were carried out at the Laboratório Nacional de Luz Síncrotron (LNLS), Campinas, Brazil. The L_3 x-ray-absorption (XAS) spectroscopy and the RPES techniques were done at the soft X-ray spectroscopy (SXS) [25] beamline, using photon energies greater than 2500 eV. At these energies, the photoelectron escape depth is large enough [26] to make the signal bulk sensitive. The overall energy resolution was about 0.3 eV. All spectra were acquired at room temperature and with the base pressure around 1×10^{-9} mbar. The samples were scraped in a vacuum, with a diamond file, to remove any surface contamination. Finally, the Fermi level and energy scale were calibrated using a clean Au foil.

III. CALCULATION DETAILS

A. Extended cluster model

The experimental spectra were compared to an extended cluster model calculation based on a (TMO_6) octahedron with a central TM ion surrounded by six oxygen O^{2-} ions in O_h symmetry [27]. All relevant charge fluctuations are considered: (i) between TM $4d$ and O $2p$ ions (for all compounds); (ii) the contribution of the coherent electrons (metallic character for molybdenum and ruthenium oxides); and (iii) between neighboring Mo ions (dimers in the MoO_2 monoclinic structure). The cluster was solved with the standard configuration-interaction method [27]: The ground states (N electrons) and excited states [$N - 1$ and $N + 1$ electrons for removal states (RSs) and addition states (ASs), respectively] were expanded beyond the purely ionic d^n in $d^{n+1}\underline{L}$, $d^{n+2}\underline{L}^2$, etc., configurations, where \underline{L} denotes a hole at the ligand (O $2p$) band [28], corresponding to the ligand screening channel (i) cited above. The Hamiltonian includes the on-site d - d Coulomb repulsion U , the p - d charge-transfer energy Δ , and the p - d transfer integrals $pd\sigma$ and $pd\pi$. The multiplet splitting, in octahedral symmetry, is given in terms of the crystal-field parameter $10Dq$, the intra-atomic exchange J , and the p - p transfer integral $pp\sigma$ - $pp\pi$.

For the metallic compounds, both ground and excited states were further expanded in the $d^{n+1}\underline{C}$, $d^{n+2}\underline{LC}$, etc., configurations (\underline{C} relates to a hole at the coherent band). The extra intercluster parameters included are the coherent charge-transfer energy Δ^* and the effective transfer integral T^* . This type of charge fluctuation represents the effective interactions of a single TMO_6 cluster with the other TMO_6 octahedra in the lattice [29], which was shown to be equivalent to a periodic p - d model [30] and was already used to describe several other metallic compounds [18,19,31]. A recent description [18] of the electronic structure of MoO_2 with an extended cluster model showed the importance of including a Mo-Mo nonlocal fluctuation to reproduce the Mo-Mo dimerization effect, which gives rise to the so-called $d_{||}$ band. Thus, the basis

set for MoO_2 also includes configurations such as $d^{n+1}\underline{D}$, $d^{n+2}\underline{LD}$, $d^{n+2}\underline{CD}$, $d^{n+3}\underline{LCD}$, etc. (\underline{D} represents a hole at the neighboring Mo ion), with the following extra intercluster parameters: $\Delta' = E(d^{n+1}:d^{n-1}) - E(d^n:d^n) = U$ (the Hubbard charge-transfer energy) and T' (the effective dimer transfer integral). The spectral weight is then calculated using the sudden approximation [32]

$$A(\omega) = \sum_j |\langle \psi_F^j | \hat{O}_F | \psi_{\text{GS}} \rangle|^2 \delta[\omega \pm (E_F^j - E_{\text{GS}})], \quad (1)$$

where $|\psi_{\text{GS}}\rangle$ represents the ground-state wave function, $|\psi_F^j\rangle$ denotes the j th eigenstate of the final state (RS or AS), E_{GS} and E_F^j are their corresponding eigenenergies, and \hat{O}_F denotes a transition operator that corresponds to the appropriate experimental technique. The resulting discrete transitions are then convoluted with Gaussian functions.

B. Resonant photoemission

To treat the RPES, we used a combination of the extended cluster with the expression developed by Davis and Feldkamp [33]. The transition amplitude, $D_k(h\nu)$, as a function of the photon energy $h\nu$ is given by

$$D_k(h\nu) = -\pi \langle \psi_{\text{RS}}^k | \hat{T} | \psi_{\text{GS}} \rangle - \pi \sum_m \left[\frac{\pi \bar{V}_{km}(h\nu) / \Gamma_m(h\nu)}{z_m(h\nu) + i\pi} [q_m(h\nu) - i] \times \sum_{k'} \bar{V}_{k'm}^*(h\nu) \langle \psi_{\text{RS}}^{k'} | \hat{T} | \psi_{\text{GS}} \rangle \right]. \quad (2)$$

In Eq. (2), the first and second terms represent the direct and indirect photoemission channels, respectively. ψ_{RS}^k corresponds to the cluster k th removal final state, \hat{T} is the removal operator of a d electron, and $\bar{V}_{km}(h\nu)$'s are the Coster-Kronig matrix elements between the addition (ψ_{AS}^m) and removal (ψ_{RS}^k) states, achieved by the $2p \rightarrow 4d$ absorption, followed by an Auger-like decay. $\Gamma_m(h\nu)$ is a typical width, proportional to $|\bar{V}_{km}(h\nu)|^2$, which represents the strength of discrete-final-state interaction, and $z(h\nu)$ is a real function [13]. Finally,

$$q_m(h\nu) = \frac{\langle \psi_{\text{AS}}^m | \hat{T}^\dagger | \psi_{\text{GS}} \rangle}{\pi \bar{V}_{km}(h\nu) \langle \psi_{\text{RS}}^k | \hat{T} | \psi_{\text{GS}} \rangle} \quad (3)$$

is the parameter related to the ratio between the absorption $\langle \psi_{\text{AS}}^m | \hat{T}^\dagger | \psi_{\text{GS}} \rangle$ (\hat{T}^\dagger is the addition operator of a d electron) and photoemission $\langle \psi_{\text{RS}}^k | \hat{T} | \psi_{\text{GS}} \rangle$ amplitudes, which generates the Fano profile [9]. Finally, the RPES signal $A_{\text{RPES}}(\omega, h\nu)$ can be obtained with

$$A_{\text{RPES}}(\omega, h\nu) = \sum_k |D_k(h\nu)|^2 \delta[\omega + (E_{\text{RS}}^k - E_{\text{GS}})], \quad (4)$$

as the interference between the direct and indirect photoemission channels in $D_k(h\nu)$ becomes responsible for the resonance effects.

TABLE I. Extended cluster model parameters for Rh₂O₃, RuO₂, and MoO₂ (all values in eV).

Parameter	Rh ₂ O ₃	RuO ₂	MoO ₂
U	4.7	4.8	3.4
Δ	1.4	0.97	5.9
$pd\sigma$	1.5	2.0	2.0
$10Dq$	1.8	2.7	2.7
J	0.25	0.70	0.41
$pp\sigma$ - $pp\pi$	1.1	0.68	0.80
Δ^*		0.61	0.56
T^*		0.20	0.08
Δ'			3.4
T'			2.1

IV. RESULTS

A. Parameters and ground-state properties

Table I presents the parameters used in the present extended cluster model calculations. The relative values of Δ and U would indicate that both Rh₂O₃ and RuO₂ ($\Delta > U$) are in the CT regime [34], whereas MoO₂ ($\Delta < U$) would appear to be in the Mott-Hubbard regime [34,35]. Further, the relatively large values of $pd\sigma$ indicate a strong covalent TM $4d$ -O $2p$ character for all compounds, which, together with the high $10Dq$ parameter, are characteristic of TM $4d$ compounds [36]. Because the intra-atomic parameter J affects mostly the x-ray-absorption spectral shape, rather than the valence-band spectra, the current values for J were obtained by reproducing the O $1s$ x-ray-absorption spectra with the corresponding cluster calculations [37]. The coherent screening parameters Δ^* and T^* for RuO₂ and MoO₂ are consistent with their metallic character and in line with previous studies [18,21]. In MoO₂, the large value for T' is due to the dimerization that occurs between neighboring Mo⁴⁺ ions. Overall, the parameters for RuO₂ and MoO₂ are in good agreement with those reported in similar materials [8,21], but no previous cluster model studies were found for the Rh₂O₃ compound.

Table II presents the main contributions to the ground state of Rh₂O₃, RuO₂, and MoO₂. In the rhodium and ruthenium oxides, the ground state is mostly attributed to the screened $d^7\bar{L}$ and $d^5\bar{L}$ configurations, respectively. Both compounds also have important contributions of the unscreened (d^6 and d^4) and well-screened ($d^8\bar{L}^2$ and $d^6\bar{L}^2$) configurations and are

said to be in an *effective negative charge-transfer* regime. This happens because the effective charge-transfer energy, between the $d^{n+1}\bar{L}$ and d^n configurations, becomes negative after the inclusion of multiplet effects ($\Delta_{\text{eff}} = \Delta + E_{\text{mult}}$). Similar results were already proposed in the description of the SrRuO₃ oxide [21].

On the other hand, the ground state of MoO₂ is mainly related to the unscreened d^2 configuration, although the screened $d^3\bar{L}$ is also quite important. This is related to the relatively high TM $4d$ -O $2p$ hybridization, represented by the $pd\sigma$ parameter. Thus, MoO₂ is said to be in a *highly mixed Mott-Hubbard* regime. Unlike the other two cases, for molybdenum oxide, there are also relevant contributions with Hubbard screening ($d^3\bar{D}$ and $d^4\bar{L}\bar{D}$) associated with the dimer T' transfer integral.

The main effect for ground states presenting such a relevant contribution from screened configurations is the high d -electron count. These values, also presented in Table II, are much higher when compared to their expected ionic values of d^6 (Rh₂O₃), d^4 (RuO₂), and d^2 (MoO₂). Further, the assignment of these regimes is important to infer on the energy scales of different charge fluctuations in each system, ultimately affecting the interpretation of our RPES results, which are shown below.

B. Spectral weight

Figure 1 presents the calculated spectral weight of Rh₂O₃, RuO₂, and MoO₂. The total spectra (in black) are a combination of the cluster model removal ($N - 1$, negative energies) and addition ($N + 1$, positive energies) states, given by Eq. (1), which are also separated into the TM $4d$ and O $2p$ contributions. Thus, the zero in the energy scale can be somewhat interpreted as the Fermi energy (E_F).

Rh₂O₃ is classified as a semiconductor with an experimental direct or indirect band-gap value of around 1.2 or 3.4 eV, respectively [38,39]. The gap of ≈ 4.0 eV calculated via the cluster model, between the filled Rh t_{2g} and empty Rh e_g subbands, presented in the top panel of Fig. 1, is close to the experimental result. The O $2p$ and Rh $4d$ bands are located from -11.5 to -4.0 eV and from -4.0 to 4.0 eV, respectively, although there is a high metal/oxygen mixture, especially within the O $2p$ band. The Rh $4d$ satellite structure, characteristic of charge-transfer regimes, is located at the bottom of the valence band (≈ -10.4 eV). Upon inspecting the composition

TABLE II. Main contributions for the ground state and d -electron count of Rh₂O₃, RuO₂, and MoO₂.

Rh ₂ O ₃		RuO ₂		MoO ₂	
Config.	(%)	Config.	(%)	Config.	(%)
$d^7\bar{L}$	52	$d^5\bar{L}$	49	d^2	43
d^6	29	$d^6\bar{L}^2$	26	$d^3\bar{L}$	35
$d^8\bar{L}^2$	17	d^4	21	$d^3\bar{D}$	9
		$d^5\bar{C}$	<1	$d^4\bar{L}^2$	7
				$d^4\bar{L}\bar{D}$	5
				$d^3\bar{C}$	<1
		TM d -electron count			
6.9		5.1		2.7	

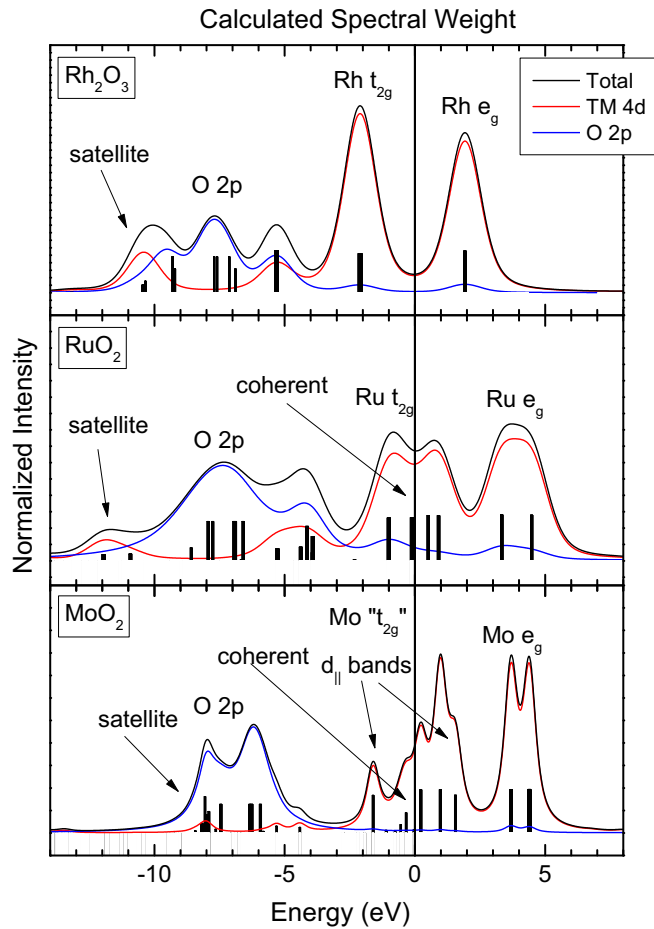


FIG. 1. Total and partial spectral weight calculated via the extended cluster model of Rh_2O_3 , RuO_2 , and MoO_2 . Black bars represent the discrete final RS and AS, which are convoluted with a Gaussian function.

of the removal final states, which will be used to interpret the RPES results, states closer to the Fermi level are related to well-screened $d^6\bar{L}$ and $d^7\bar{L}^2$ configurations, whereas the satellite region is mainly related to poorly screened d^5 and $d^6\bar{L}$ configurations.

The middle panel of Fig. 1 shows that, for RuO_2 , the O 2p and Ru 4d bands are located from -11.5 to -2.7 eV and from -2.7 to 7.0 eV, respectively. As in the case of Rh_2O_3 , it is also possible to observe a Ru 4d satellite at the bottom of the valence band. The calculation shows that the Ru $4dt_{2g}$ subband is continuous at E_F , due to the coherent contribution to the spectra, as expected for metals. Finally, the distribution of the removal final states is similar to the previous compound. Namely, states near the Fermi level are mostly related to well-screened configurations, whereas high-energy structures are mainly due to poorly screened configurations.

For MoO_2 , the cluster model spectrum, shown in the bottom panel of Fig. 1, is again continuous at E_F , crossing the Mo $4dt_{2g}$ subband, due to metallic/coherent fluctuations. This system also presents a relatively high covalent TM $4d$ -O $2p$ mix, especially at the valence-band region. Now, the satellite structure is hidden in the bottom of the O $2p$ band and is much less relevant than in the previous compounds, a result

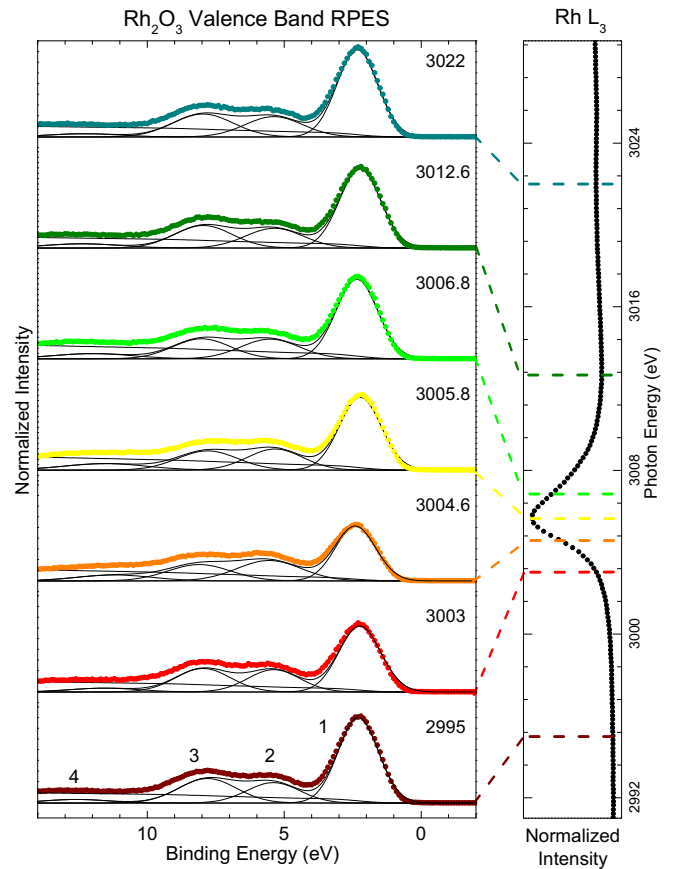


FIG. 2. Left panel: Valence-band photoemission spectra of Rh_2O_3 taken with different photon energies, as indicated in each spectrum, within the Rh L_3 absorption edge. Black solid lines correspond to the Gaussian plus integral background fit made to the main VB regions (1, 2, 3, and 4). Right panel: Rh L_3 x-ray-absorption spectrum of Rh_2O_3 .

typical for the Mott-Hubbard regime. Thus, also in contrast to the previous systems, removal states closer to the Fermi energy are now mostly formed of poorly screened configurations, whereas the higher-energy states are mainly related to well-screened features. Finally, it is important to note that in this case the Mo-Mo dimerization causes a further split within the Mo t_{2g} states, giving rise to the occupied and unoccupied parts of the so-called $d_{||}$ band.

C. L_3 resonant photoemission spectra

The left panel of Fig. 2 shows the valence-band photoemission spectra of Rh_2O_3 . Each spectrum was taken with the indicated photon energy, within the Rh L_3 ($2p_{3/2}$) absorption edge, which is shown in the right panel of Fig. 2. All valence-band spectra were divided into four regions (1, 2, 3, and 4) and fitted using Gaussian curves and an integral background (black solid lines). We note that region 1 can be linked to the Rh 4d band, regions 2 and 3 can be associated with the O 2p band, and region 4 can be related to a small satellite feature. This assignment is confirmed by the inspection of the calculated removal states of Rh_2O_3 (see Fig. 1), which reproduces the relative energy positions of these structures.

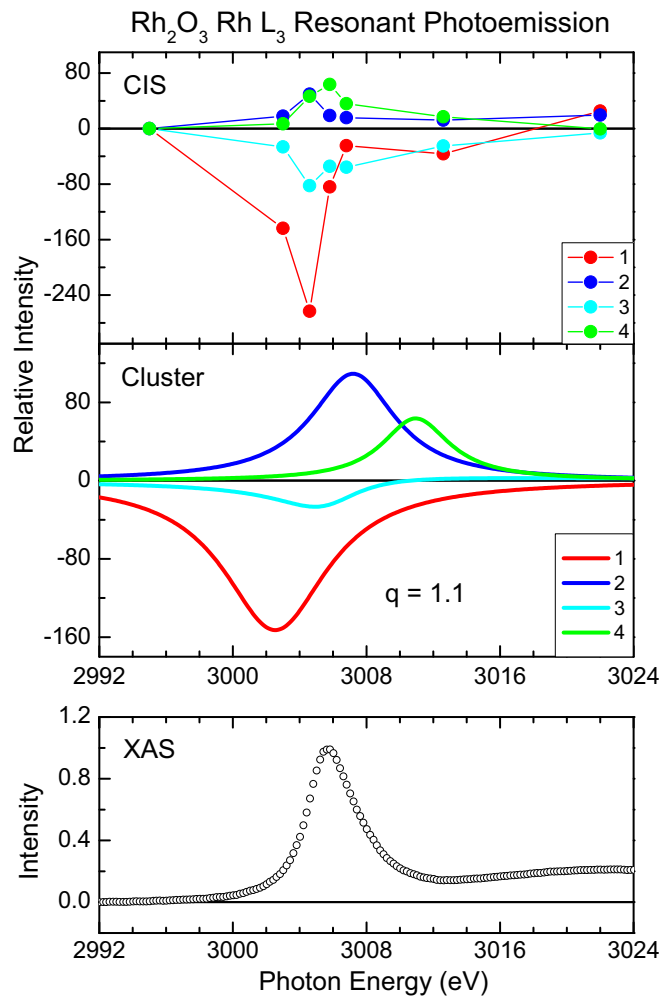


FIG. 3. Top panel: Constant initial-state (CIS) curves of Rh₂O₃ obtained from the integrated area of corresponding regions determined in Fig. 2 (lines are a guide to the eye). Middle panel: Cluster model results of Rh₂O₃ RPES calculation obtained using Eq. (4). Bottom panel: The Rh L₃ XAS is shown for comparison.

The relative integrated areas of each main region in the valence-band spectra of Rh₂O₃, as a function of the incident photon energy, are depicted in the top panel of Fig. 3. The experimental constant initial-state (CIS) spectrum clearly shows the distinct resonance behavior of each component of the valence band of Rh₂O₃. Regions 1 and 3 show a decrease in intensity as the photon energy sweeps across the Rh L₃ edge, whereas regions 2 and 4 show a relative increase.

The cluster model results are presented in the middle panel of Fig. 3. They show the relative intensity of all final removal states within each energy region of the calculated valence-band spectra [calculated according to Eq. (4)], as a function of the photon energy. In this RPES calculation, the main parameter is q , given by Eq. (3), which corresponds to a value of $q = 1.1$ for the Rh₂O₃ material. The results are in good agreement with the experimental CIS in terms of signal behavior, but we note that the effect calculated for region 1 is slightly underestimated.

The same procedure was followed for the other compounds. Left panels of Figs. 4 and 5 show the valence-band

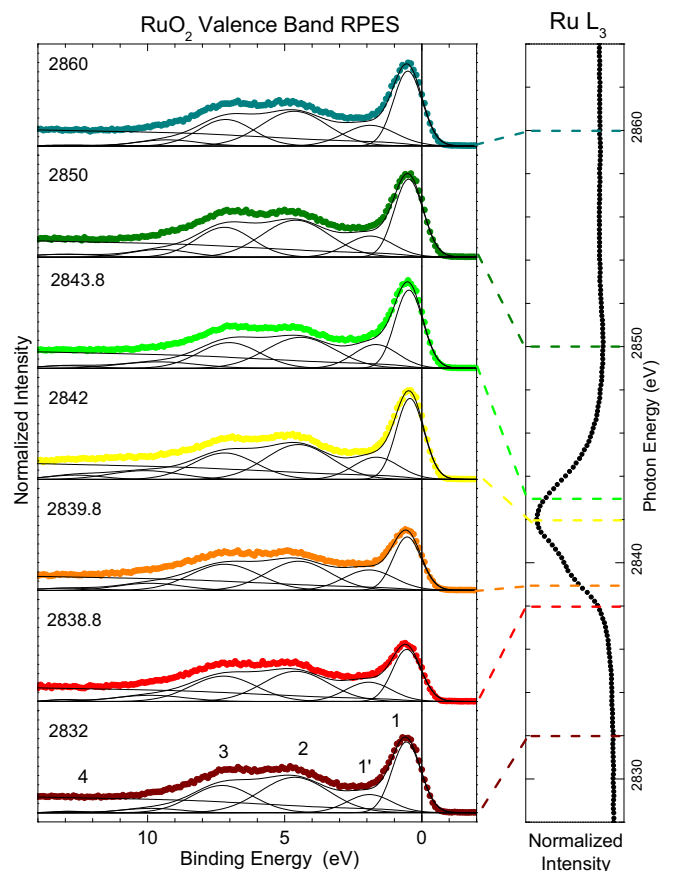


FIG. 4. Left panel: Valence-band photoemission spectra of RuO₂ taken with different photon energies, as indicated in each spectrum, within the Ru L₃ absorption edge. Black solid lines correspond to the Gaussian plus integral background fit made to the main VB regions (1, 1', 2, 3, and 4). Right panel: Ru L₃ x-ray-absorption spectrum of RuO₂.

spectra of RuO₂ and MoO₂, respectively. Each spectrum was taken with the indicated photon energy, within the Ru or Mo L₃ (2p_{3/2}) absorption edge, which is shown in the right panels of their respective figures. Further, each valence-band spectrum was again separated into different regions and fitted using Gaussian curves and an integral background.

In the case of the RuO₂ material (Fig. 4), regions 1 and 1' are related to the Ru 4d band, regions 2 and 3 are associated with the O 2p band, and region 4 can be related to a small satellite feature. Here, the double structure in the Ru 4d band can be related to the coherent (region 1) and incoherent (region 1') parts, which will be further discussed below. As for the MoO₂ oxide (Fig. 5), regions 1 and 2 are now linked to the Mo 4d band, whereas regions 3 and 4 are associated with the O 2p band. Now, the double structure in the TM band is attributed to the dimerization effect ($d_{||}$ band split), while no evident satellite is present in this case. Finally, these assignments are corroborated by the calculated removal states of RuO₂ and MoO₂ (see Fig. 1), which reproduces the relative energy positions of these features.

The experimental CIS spectrum of RuO₂ is presented in the top panel of Fig. 6. The resonance behavior across the Ru L₃ edge is again distinct for each region in the valence band,

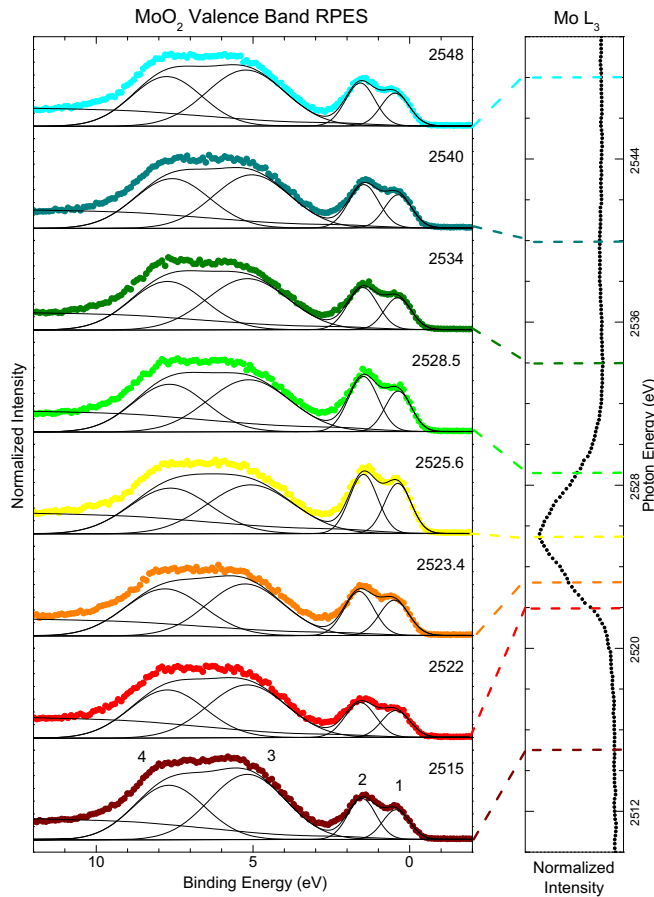


FIG. 5. Left panel: Valence-band photoemission spectra of MoO_2 taken with different photon energies, as indicated in each spectrum, within the $\text{Mo } L_3$ absorption edge. Black solid lines correspond to the Gaussian plus integral background fit made to the main VB regions (1, 2, 3, and 4). Right panel: $\text{Mo } L_3$ x-ray-absorption spectrum of MoO_2 .

exhibiting a clear decrease or increase in the relative intensity. More specifically, we note that the CIS spectra of regions 1 and 1', within the $\text{Ru } 4d$ band, present contrasting profiles, indicating different screening mechanisms. Thus, these regions can be attributed to the coherent and incoherent parts of the TM band, respectively, in similar fashion to what was found in the SrRuO_3 compound [21]. The cluster model calculations for RuO_2 are shown in the middle panel of Fig. 6, with the q parameter again equal to $q = 1.1$. The results also reproduce the experimental CIS with an overall good agreement, even though the resonance effects for region 1 are much higher. As we will expand upon in the following section, the general shape of a CIS curve is dictated by the screening mechanism in that energy region. Therefore, this feature of the cluster model could be attributed to an overestimation of such charge fluctuation contribution in the $\text{Ru } 4d$ band.

Finally, the experimental CIS spectrum of MoO_2 is presented in the top panel of Fig. 7. The resonance effects throughout the $\text{Mo } L_3$ edge show an increase (decrease) in the intensity of lower (higher) binding-energy regions. The cluster model calculations for MoO_2 are shown in the middle panel of Fig. 7, with the q parameter now equal to $q = 1.0$. The

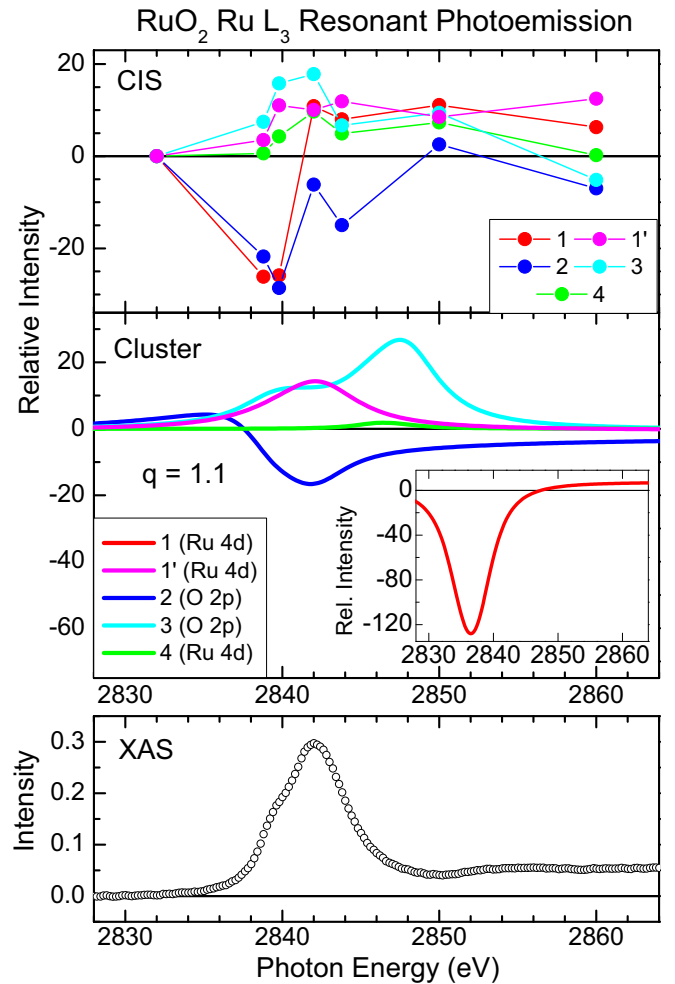


FIG. 6. Top panel: CIS curves of RuO_2 obtained from the integrated area of corresponding regions determined in Fig. 4 (lines are a guide to the eye). Middle panel: Cluster model results of RuO_2 RPES calculation obtained using Eq. (4). Bottom panel: The $\text{Ru } L_3$ XAS is shown for comparison.

results also reproduce the overall shape of the experimental CIS, despite a small decrease in intensity predicted to region 1, which does not appear in the experiment.

V. DISCUSSION

In previous reports, Guedes *et al.* [21] and Martins *et al.* [8] also studied the resonance behavior in the L_3 RPES of other $4d$ oxides. They measured the photoemission spectra with photons corresponding to on- and off-resonance energies. In the former, the on-off spectrum was directly related to the TM $4d$ character in the valence band, without the inclusion of interference between direct and indirect photoemission channels. In the latter, the interference process was considered, but ground-state band-structure calculations were used as the input for the comparison. In the present paper, the extended cluster model considers all the relevant charge-transfer fluctuations and correlation effects to calculate the ground and final states involved in the RPES technique, and also considers the interference between those different final-state transitions.

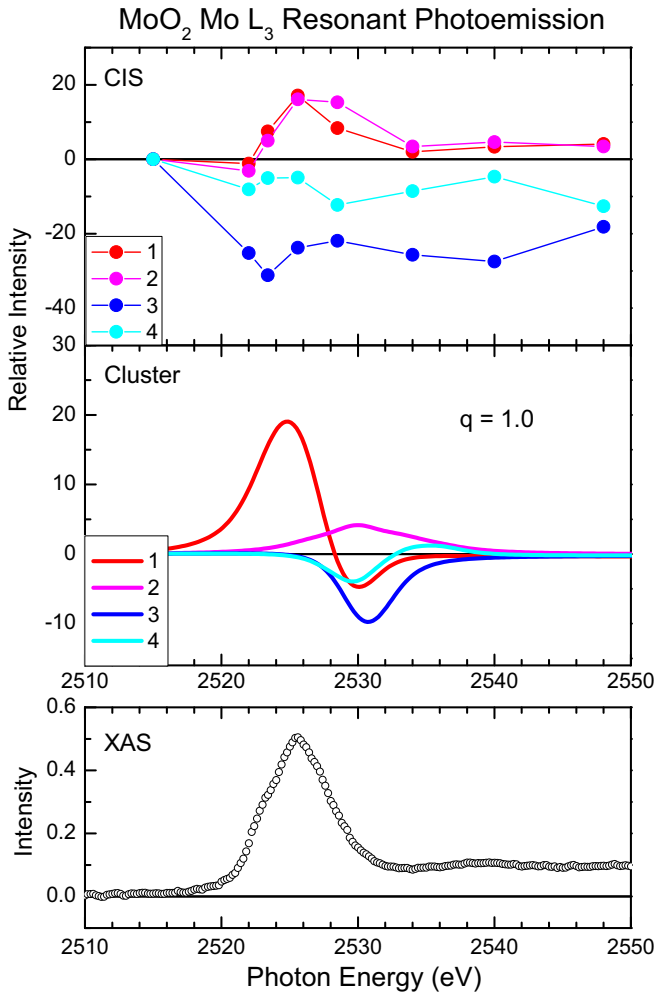


FIG. 7. Top panel: CIS curves of MoO₂ obtained from the integrated area of corresponding regions determined in Fig. 5 (lines are a guide to the eye). Middle panel: Cluster model results of MoO₂ RPES calculation obtained using Eq. (4). Bottom panel: The Mo L₃ XAS is shown for comparison.

At a first glance, it feels quite unusual that the diverse resonance behaviors for each compound were reproduced with such similar values of the q parameter. To check the validity of these parameters, we also calculated q as per Ref. [14]. In this paper, q is given in terms of the photoemission dipole $\langle \epsilon p | r | 4d \rangle$ and $\langle \epsilon f | r | 4d \rangle$ matrix elements, the absorption dipole $\langle 4d | r | 2p \rangle$ matrix element, and the Auger $R^{1,3}(2p, \epsilon p; 4d, 4d)$ and $R^{1,3}(2p, \epsilon f; 4d, 4d)$ integrals, which were calculated here using the code by Cowan [40]. These are, in turn, presented in Table III. As one can see, the values of the q parameter are also remarkably close for all compounds. The larger magnitude obtained in this atomlike Hartree-Fock calculation, when comparing to the cluster model results, can be related to further screening presented in the solid, which would eventually imply a reduction of these parameters. Therefore, the different behaviors in the calculated RPES must be attributed to another effect, as we discuss below.

Upon inspecting the TM $4d$ spectral weight of Rh₂O₃ (see Fig. 1), one could naively expect that the resonance curve corresponding to region 1 would show the largest

TABLE III. Dipole matrix elements (in atomic units) and radial integrals (in Ry) calculated using the code by Cowan [40]. The corresponding values of q are shown in the last line.

Parameter	Rh ₂ O ₃	RuO ₂	MoO ₂
$\langle 4d r 2p \rangle$	-0.021	-0.022	-0.023
$\langle \epsilon p r 4d \rangle$	0.00024	0.00025	0.00027
$\langle \epsilon f r 4d \rangle$	-0.0012	-0.0013	-0.0014
$R^1(2p, \epsilon p; 4d, 4d)$	-0.0027	-0.0028	-0.0025
$R^1(2p, \epsilon f; 4d, 4d)$	0.0083	0.0086	0.0078
$R^3(2p, \epsilon p; 4d, 4d)$	-0.0023	-0.0023	-0.0021
$R^3(2p, \epsilon f; 4d, 4d)$	0.0052	0.0054	0.0048
q	3.1	2.9	3.1

intensity enhancement in the RPES technique. Instead, it presents a very pronounced dip, as we can see from Fig. 3. The reason for such behavior comes from the type of regime to which Rh₂O₃ is subject to. As mentioned in Sec. IV B, there is a huge presence of well-screened states next to E_F in charge-transfer regime compounds, which is justified by the relatively small value of Δ . Alternatively, the intensity enhancement of structures inside the O $2p$ band region can be related to the high value of Coulomb repulsion U , which makes unscreened and poorly screened states appear at higher binding-energy regions.

The RuO₂ case is similar to Rh₂O₃ because both are in the same CT regime, where the negative value of Δ_{eff} makes the low binding-energy region exhibit a strong TM $4d$ -O $2p$ mixture. Usually, this regime can be confirmed by the presence of high binding-energy satellites in core-level or valence-band photoemission spectra. Because of the high photon energy and consequently small photoionization cross section, these are subdued in Figs. 2 and 4. But, in spectra taken with lower photon energies, these satellite intensities are more prominent [41]. Observing Fig. 6, and comparing it with the rhodium oxide, we can see an alternating RPES signal of curves 2 and 3 (inside O $2p$ band). This effect could be associated with nonlocal (coherent) fluctuations that are present in RuO₂ but absent in Rh₂O₃. Although the Δ^* value is small compared to U , adding a second type of screening can cause energy rescaling of the different removal final states, moving them away from or closer to E_F , depending on their relative contributions.

For MoO₂, because of the Mott-Hubbard regime, low binding-energy states are largely composed of unscreened or poorly unscreened configurations. Therefore, there are more “pure metallic states” closer to E_F in molybdenum oxide. So, it makes sense that the resonance curves corresponding to regions 1 and 2 of the valence band present a more accentuated increase than those related to the remaining parts of the spectra (see Fig. 7). The relatively large Δ value, in this case, shifts oxygen well-screened states to higher binding energies.

These observations are in agreement with the reports from Davis [15] and Fujimori and Minami [17], who studied RPES in TM $3d$ compounds. Succinctly, structures which have higher screening from oxygen should present a small positive or negative resonance in the valence band of TMO’s. In contrast, features with a more pure TM character (unscreened) manifest a higher positive enhancement in their resonance curve, and the CT regime, in which the compound is found,

controls the positions of such states within the valence band (close to or far from E_F , for example). Therefore, the inclusion of the essential charge fluctuations in the description of the electronic structure of a given system is of great importance to correctly account for the partial contributions in valence-band states.

VI. CONCLUSIONS

In summary, we reported experimental L_3 resonant photoemission of Rh_2O_3 , RuO_2 , and MoO_2 . Also, we have applied a combination of Fano's theory with an extended cluster model which was able to reproduce the essential features of RPES involving Coster-Kronig transitions in these $4d$ transition-metal oxides. The resonance enhancement of the satellites, rather than the main lines, illustrated by the CIS curves for rhodium and ruthenium oxides, at the L_3 absorption edge, is attributed partly to covalence and partly to the charge-transfer regime

to which these compounds are subjected. The Mott-Hubbard regime for MoO_2 causes main line resonance to enhance more than for satellite structures since well-screened states are localized at higher binding energies. In addition to the good agreement with the CIS curves, our extended cluster model reproduced qualitatively the results for the resonant parameter q obtained via the Hartree-Fock method, which corroborate the accuracy of the results of our extended cluster model.

ACKNOWLEDGMENTS

This work was supported by Brazilian funding agencies FAPESP (Grants No. 2013/07296-2 and No. 2019/26141-6), CAPES, and CNPq (Grants No. 307153/2016-9, No. 306783/2019-3, and No. 301463/2019-0). We acknowledge SXS beamline staff for technical support and the CNPEM/LNLS for granting beam time under Project No. SXS-20150121.

-
- [1] S. Grebinkij, M. Senulis, H. Tvardauskas, V. Bondarenkaa, V. Lissauskas, B. Vengalis, B. Orlowski, R. Johnson, and S. Mickevičius, *Radiat. Phys. Chem.* **80**, 1140 (2011).
- [2] C. Guillot, Y. Ballu, J. Paigné, J. Lecante, K. P. Jain, P. Thiry, R. Pinchaux, Y. Pétrouff, and L. M. Falicov, *Phys. Rev. Lett.* **39**, 1632 (1977).
- [3] A. Tanaka and T. Jo, *J. Phys. Soc. Jpn.* **63**, 2788 (1994).
- [4] Z. Zhang, S. P. Jeng, and V. E. Henrich, *Phys. Rev. B* **43**, 12004 (1991).
- [5] R. L. Kurtz, R. L. Stockbauer, D. Mueller, A. Shih, L. E. Toth, M. Osofsky, and S. A. Wolf, *Phys. Rev. B* **35**, 8818 (1987).
- [6] R. Eguchi, M. Taguchi, M. Matsunami, K. Horiba, K. Yamamoto, Y. Ishida, A. Chainani, Y. Takata, M. Yabashi, D. Miwa, Y. Nishino, K. Tamasaku, T. Ishikawa, Y. Senba, H. Ohashi, Y. Muraoka, Z. Hiroi, and S. Shin, *Phys. Rev. B* **78**, 075115 (2008).
- [7] J. Laverock, B. Chen, K. E. Smith, R. P. Singh, G. Balakrishnan, M. Gu, J. W. Lu, S. A. Wolf, R. M. Qiao, W. Yang, and J. Adell, *Phys. Rev. Lett.* **111**, 047402 (2013).
- [8] H. P. Martins, F. Prado, A. Caneiro, F. C. Vicentin, R. J. O. Mossaneck, and M. Abbate, *Europhys. Lett.* **118**, 37002 (2017).
- [9] U. Fano, *Phys. Rev.* **124**, 1866 (1961).
- [10] R. E. Dietz, E. G. McRae, Y. Yafet, and C. W. Caldwell, *Phys. Rev. Lett.* **33**, 1372 (1974).
- [11] E. J. McGuire, *Phys. Rev. A* **5**, 1043 (1972).
- [12] R. Bruhn, B. Sonntag, and H. W. Wolff, *Phys. Lett. A* **69**, 9 (1978).
- [13] L. C. Davis and L. A. Feldkamp, *Phys. Rev. B* **15**, 2961 (1977).
- [14] L. C. Davis and L. A. Feldkamp, *Phys. Rev. B* **23**, 6239 (1981).
- [15] L. C. Davis, *Phys. Rev. B* **25**, 2912 (1982).
- [16] S. J. Oh, J. W. Allen, I. Lindau, and J. J. C. Mikkelsen, *Phys. Rev. B* **26**, 4845 (1982).
- [17] A. Fujimori and F. Minami, *Phys. Rev. B* **30**, 957 (1984).
- [18] V. Stoeberl, M. Abbate, L. M. S. Alves, C. A. M. dos Santos, and R. J. O. Mossaneck, *J. Alloys Compd.* **691**, 138 (2017).
- [19] R. J. O. Mossaneck and M. Abbate, *Phys. Rev. B* **74**, 125112 (2006).
- [20] M. Abbate, R. Potze, G. A. Sawatzky, and A. Fujimori, *Phys. Rev. B* **49**, 7210 (1994).
- [21] E. B. Guedes, M. Abbate, K. Ishigami, A. Fujimori, K. Yoshimatsu, H. Kumigashira, M. Oshima, F. C. Vicentin, P. T. Fonseca, and R. J. O. Mossaneck, *Phys. Rev. B* **86**, 235127 (2012).
- [22] J. W. M. Biesterbos and J. Hornstra, *J. Less-Common Met.* **30**, 121 (1973).
- [23] T. Takeda, M. Nagata, H. Kobayashi, R. Kanno, Y. Kawamoto, M. Takano, T. Kamiyama, F. Izumi, and A. W. Sleight, *J. Solid State Chem.* **140**, 182 (1998).
- [24] A. A. Bolzan, B. J. Kennedy, and C. J. Howard, *Aust. J. Chem.* **48**, 1473 (1995).
- [25] M. Abbate, F. C. Vicentin, V. Compagnon-Cailhol, M. C. Rocha, and H. Tolentino, *J. Synchrotron Radiat.* **6**, 964 (1999).
- [26] J. Zemek, S. Hucek, A. Jablonski, and I. Tilinin, *J. Electron Spectrosc. Relat. Phenom.* **76**, 443 (1995).
- [27] V. A. Dzuba, V. V. Flambaum, and M. G. Kozlov, *Phys. Rev. A* **54**, 3948 (1996).
- [28] M. Imada, A. Fujimori, and Y. Tokura, *Rev. Mod. Phys.* **70**, 1039 (1998).
- [29] R. J. O. Mossaneck, M. Abbate, T. Yoshida, A. Fujimori, Y. Yoshida, N. Shirakawa, H. Eisaki, S. Kohno, P. T. Fonseca, and F. C. Vicentin, *Phys. Rev. B* **79**, 033104 (2009).
- [30] P. Lombardo, M. Avignon, J. Schmalian, and K.-H. Bennemann, *Phys. Rev. B* **54**, 5317 (1996).
- [31] G. Panaccione, M. Altarelli, A. Fondacaro, A. Georges, S. Huotari, P. Lacovig, A. Lichtenstein, P. Metcalf, G. Monaco, F. Offi, L. Paolasini, A. Poteryaev, M. Sacchi, and O. Tjernberg, *Phys. Rev. Lett.* **97**, 116401 (2006).
- [32] T. Saitoh, A. E. Bocquet, T. Mizokawa, H. Namatame, A. Fujimori, M. Abbate, Y. Takeda, and M. Takano, *Phys. Rev. B* **51**, 13942 (1995).
- [33] L. C. Davis and L. A. Feldkamp, *Phys. Rev. A* **24**, 1862 (1981).
- [34] J. Zaanen, G. A. Sawatzky, and J. W. Allen, *Phys. Rev. Lett.* **55**, 418 (1985).
- [35] A. Fujimori, T. Yoshida, K. Okazaki, T. Tsujioka, K. Kobayashi, T. Mizokawa, M. Onoda, T. Katsufuji, Y. Taguchi, and Y. Tokura, *J. Electron Spectrosc. Relat. Phenom.* **117**, 277 (2001).
- [36] Y. S. Lee, J. S. Lee, T. W. Noh, D. Y. Byun, K. S. Yoo, K. Yamaura, and E. Takayama-Muromachi, *Phys. Rev. B* **67**, 113101 (2003).

- [37] V. Stoerberl, Ph.D. thesis, Universidade Federal do Paraná, 2020.
- [38] J. Ghose and A. Roy, *AIP Conf. Proc.* **370**, 901 (1996).
- [39] F. P. Koffyberg, *J. Phys. Chem. Solids* **53**, 1285 (1992).
- [40] R. D. Cowan, *The Theory of Atomic Structure and Spectra* (University of California, Berkeley, 1981).
- [41] V. Stoerberl, E. B. Guedes, M. Abbate, F. Abud, R. F. Jardim, and R. J. O. Mossaneck, 2020 (unpublished).